Annealing-time and annealing-temperature dependencies of the size of Ni-Mn-In shell-ferromagnetic nano-precipitates by Scherrer analysis

Cite as: AIP Advances **8**, 025012 (2018); https://doi.org/10.1063/1.5018851
Submitted: 10 December 2017 . Accepted: 07 February 2018 . Published Online: 15 February 2018

L. Dincklage, F. Scheibel, A. Çakır, M. Farle, M. Acet, et al.

Annealing-time and annealing-temperature dependencies of the size of Ni-Mn-In shell-ferromagnetic nano-precipitates by Scherrer analysis

L. Dincklage,[1] F. Scheibel,[1] A. Çakır,[1,2] M. Farle,[1,3] and M. Acet[1,a]
[1]*Faculty of Physics, University of Duisburg-Essen, 47057 Duisburg, Germany*
[2]*Department of Metallurgical and Materials Engineering, Muğla Sıtkı Koçman University, 48000 Mugla, Turkey*
[3]*Center for FunMagMa, Immanuel Kant Baltic Federal University, 236041 Kaliningrad, Russian Federation*

(Received 10 December 2017; accepted 7 February 2018; published online 15 February 2018)

Shell-ferromagnetic effects are observed in Ni-Mn-based off-stoichiometric Heuslers decomposed into ferromagnetic precipitates embedded in an antiferromagnetic matrix when the surface-to-volume ratio of the precipitates are sufficiently large. However, since the size of the precipitates have until now not been determined, it is not known which ratios are involved. Here we carry out a Scherrer analysis on decomposed specimens to determine the precipitate-size as a function of decomposition temperature and time. https://doi.org/10.1063/1.5018851

Off-stoichiometric Ni-Mn-based Heuslers with composition $Ni_{50}Mn_{50-x}Z_x$ (Z: Al, Ga, In, Sn, Sb) are multifunctional materials undergoing magnetostructural martensitic transitions[1] and have potential applications in the areas of magnetic shape-memory,[2,3] magnetocalorics,[4,5] and giant magnetoresistance;[6] all particularly in the room temperature range. In addition to multifunctionalities, these alloys are also interesting for studying basic physical phenomena such as kinetic arrest[7,8] and intrinsic exchange bias;[9–11] as these phenomena can relate their complex, mixed-magnetic interactions at the microscopic scale precisely to their multifunctional capabilities at the macroscopic scale.

However, there is one property of these off-stoichiometric alloys that has been largely overlooked when dealing with their multifunctionalities: These alloys decompose into cubic ($L2_1$) ferromagnetic (FM) $Ni_{50}Mn_{25}Z_{25}$ and tetragonal ($L1_0$) antiferromagnetic (AF) $Ni_{50}Mn_{50}$ components when annealed in the temperature-range $600 \leq T_a \leq 750$ K.[12–17] The uncertainties in the metallurgical state of the studied samples caused by the decomposition occurring during various sample preparation processes, such as annealing and quenching, can have major consequences on the interpretation of the obtained data. Alone in this respect, studying the decomposition properties of these alloys is vital to the understanding of their multifunctional properties.

On the other hand, the decomposition itself opens up a new dimension in the palette of multifunctionalities in these alloys. A particularly interesting situation occurs when $x = 5$ and the sample is annealed at $T_a \approx 650$ K while a magnetic-field $B \approx 100$ mT is applied. In this case, the resulting FM component consists of nanometer-sized shell-FM precipitates embedded in an AF matrix. The AF matrix causes the shell-spins of the precipitates to strongly pin in the direction of the applied field during decomposition, whereas the core-spins are 'loose'. The consequences of the shell-FM effect can be viewed at online videos.[18,19] The Curie temperature T_C of the core is about 320 K which corresponds to that of $L2_1Ni_{50}Mn_{25}Z_{25}$; T_C being nearly independent of the Z-element. The shell spins are so strongly pinned that they show vertically shifted minor hysteresis loop such that the the remanent magnetizations of the loops are always positive.[21–23] At room temperature, the spins begin

[a]mehmet.acet@uni-due.de

to flip only in fields exceeding 9 T, and their remanent configuration is maintained up to nearly the minimum decomposition temperature of 600 K.[24]

It is thought that the shell-FM effect is observable when the surface-to-volume ratio of the precipitates are sufficiently large. If the precipitate grows too large, the volume becomes large, and the shell-FM effect becomes masked. However, since the size of the precipitates have until now not been determined, it is not known which ratios are involved for the effect to be observable, and therefore, what the optimum ratio would be. Here, we carry out a Scherrer analysis on decomposed specimens to determine the precipitate-size as a function of decomposition temperature and time on $Ni_{50}Mn_{50-x}In_5$ decomposed at various T_a for various annealing times t_a.

The sample was prepared by arc melting followed by quartz-glass-encapsulation under 300 mbar Ar and annealing at 1073 K for 5 days. It was then quenched in water at room temperature. The composition of the sample was determined by energy dispersive x-ray analysis to be $Ni_{48.13}Mn_{46.57}Mn_{5.30}$ (nominal: $Ni_{50}Mn_{45}In_5$). The ingot was then ground to powder, passed through a 100 μm sieve, wrapped in Ta, sealed in a quartz tube and strain-annealed for a further 24 hours at 1073 K and quenched in water at room temperature. For the decomposition experiments, the powder was divided into twelve, encapsulated, and annealed at 650, 700, and 750 K each for 10^3 s (~0.3 h), 10^4 s (~2.8 h), 10^5 s (~28 h), and 10^6 s (~280 h).

X-ray diffraction (XRD) was carried out using a Panalytical X'Pert Pro diffractometer with Cu K-alpha radiation. A programmable divergence slit and a programmable receiving slit were set to illuminate and observe a 20 mm length of the sample, which was spread over a Si zero-background sample holder mounted on a spinner. A programmable receiving slit with a fixed height of 1.5 mm and a curved graphite monochromator were used before the detector. JANA2006 software was used for the refinements and the estimation of the FWHMs.[20]

In general, the broadening of the spectral lines in an XRD pattern can provide information on strain and grain size. After correcting for the instrumental broadening, the grain-size (in the present case, the precipitate-size) can be estimated from

$$D_{hkl} = \frac{k\lambda}{(FWHM)cos(\theta)_{hkl}}, \tag{1}$$

where D_{hkl} is the precipitate size (diameter), h, k, l are Miller indices, the factor k is taken as 0.89, $FWHM$ is the full-width-at-half-maximum corrected for the instrumental broadening and strain, and $(\theta)_{hkl}$ is the peak-angle. $FWHM$ can be expressed as the difference between the measured $FWHM$, $(FWHM)_{meas}$, and the contribution from both strain effects and the instrumental resolution $(FWHM)_{strain+ires}$ so that for any hkl,

$$(FWHM) = (FWHM)_{meas} - (FWHM)_{strain+ires}. \tag{2}$$

from here, D_{hkl} can be estimated by substituting eq. 2 in eq. 1.

When $Ni_{50}Mn_{45}In_5$ is annealed at around 650-750 K, cubic precipitates of $Ni_{50}Mn_{25}In_{25}$ are formed in a tetragonal $Ni_{50}Mn_{50}$ matrix described by the reaction

$$Ni_{50}Mn_{45}In_5 \rightarrow Ni_{50}Mn_{25}In_{25} + Ni_{50}Mn_{50}, \tag{3}$$

so that as the reaction progresses, peaks related to the cubic structure begin to appear. The process is shown in fig. 1. Fig. 1(a) shows the refined XRD pattern for the initial $L1_0$ tetragonal state (space group $I4mmm$). On annealing at 750 K for 10^5 s, the (400) and (422) peaks related to the cubic $L2_1$ phase appear, which are distinct and can be used for determining the precipitate-size. The refined XRD for a sample annealed at 750 K for 10^5 s is shown in fig. 1(b). In addition to the peaks associated with the initial tetragonal state (tet initial), new peaks related to a new tetragonal phase (tet new) and a cubic phase also appear. Weak intensity peaks related to MnO are also observed.

The correction of the $FWHM$ of the emerging (400) and (422) peaks for strain and instrumental resolution are made by comparing them to those of the peaks in the spectrum of a 100 μm $Ni_{50}Mn_{25}In_{25}$ reference Heusler powder-sample, which is prepared for these studies by annealing it at 800 °C for 24 h. The widths of the peaks for the reference material should be due entirely to the instrumental broadening, if the powder is strain-free. To check this, we compare the angle-dependence of

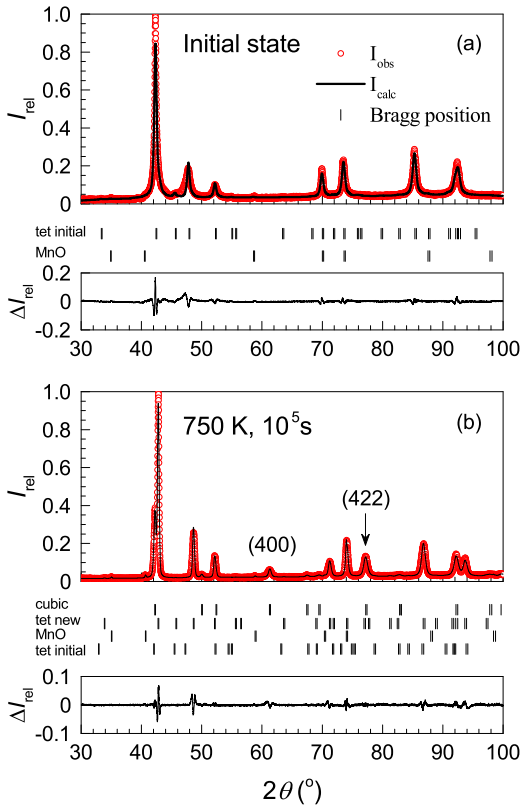

FIG. 1. Refined XRD data. (a) The initial state of $Ni_{50}Mn_{45}In_5$. (b) $Ni_{50}Mn_{45}In_5$ decomposed at 750 K for 10^5 s. The (400) and (422) peaks pertaining to the cubic precipitates are indicated with arrows. Intensities of observed, I_{obs} and calculated I_{calc} spectra and the Bragg positions of the various phases are indicated as in the legend. The difference spectra, ΔI_{rel}, are given at the bottom of each spectrum.

the *FWHM* to that of a strain-free polycrystalline Si standard (Panalytical). Fig. 2 shows that the behavior of the FWHM for $Ni_{50}Mn_{25}In_{25}$ and the Si-standard are similar but with the angle-dependence for the Heusler shifted to slightly higher values. The shift can be due to residual strain.

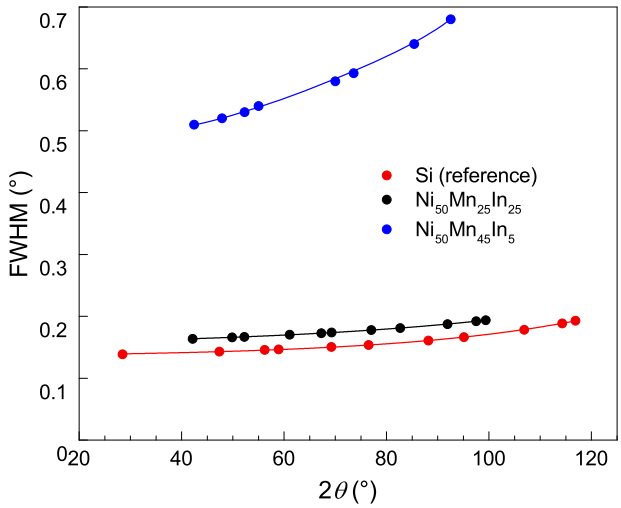

FIG. 2. *FWHM* vs 2θ for a Si reference and a $Ni_{50}Mn_{25}In_{25}$ cubic Heusler reference. The lines through the data are exponential fits.

However this amount of shift has a negligibly small effect in determining the size of the precipitates determined below. In fact the broadening for $Ni_{50}Mn_{25}In_{25}$ can be used directly for the second term in eq. 2.

Since the decomposed state is obtained by annealing at elevated temperatures, it should be in a thermodynamically more stable state than the $Ni_{50}Mn_{45}In_5$ initial state. This would suggest that the initial state, obtained by quenching from 1073 K, could be strained. By inspecting the peak profiles in fig. 1(a) one already recognizes broader peaks than for $Ni_{50}Mn_{25}In_{25}$. A plot of their FWHMs included in fig. 2 shows that the broadening is considerably greater indicating that the initial state is a strained state and that decomposition causes a release of the strain. This point is further discussed below.

The evolution of the patterns for T_a = 750 K from the initial state to an annealing time of 10^6 s is shown in fig. 3. Both the (400) and the (422) peaks of the cubic structure become narrower while gaining intensity as the annealing time increases. Similar situations are observed for T_a = 650 and 700 K.

The log(t_a)-dependence of the FWHMs are shown in fig. 4 for the three annealing temperatures. A realistic estimation could be carried out for only two annealing times at 650 and 700 K, whereas three values can be estimated for T_a = 750 K as seen in figs. 4(a)–(c). The average precipitate diameter obtained from these values are plotted in figs. 4(d)–(f) as a function of log(t_a) and T_a. Figs. 4(d) and (e) show that the values obtained from both peaks are in good agreement. In both cases, one sees that the size of the precipitate formed at 650 K does not vary as time progresses and remains at a value of about 4-5 nm. For T_a = 700 and 750 K on the other hand, the precipitate grows further with increasing time. Fig. 4(f) shows the T_a-dependence of the precipitate-size for 10^6 s annealing time obtained from both cubic peaks. The precipitate-size increases as T_a increases.

The Scherrer analysis provides only an estimate of the average size and provides no information on the actual size distribution. Microscopy studies are required for a better size determination. Nevertheless, we can observe here a systematic increase of the the size of the precipitates with increasing T_a and increasing t_a. One exception, on the other hand, that sands out is the fact that for T_a = 650 K, the particles grow to $D \approx$ 3-5 nm for $t_a = 10^5$ s and lock to this size so that practically no further growth in size takes place although the number of precipitates increase with increasing time as observed in time-dependent-magnetization measurements carried out 650 K.[24] The surface-to-volume ratio of a sphere is 3/r, where r is the radius of the sphere. The estimated ratio for precipitates with $D = 3 - 5$ nm

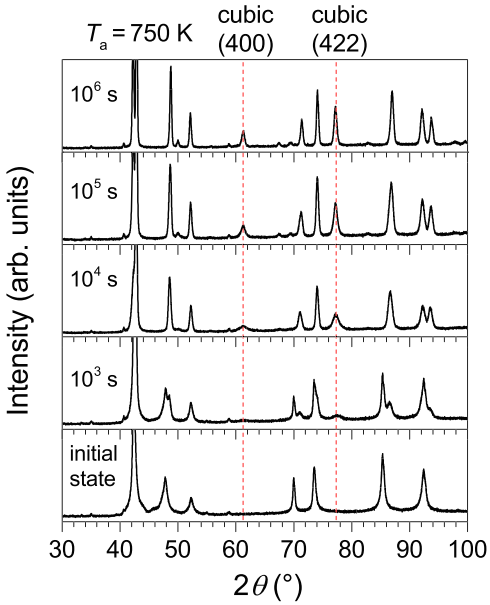

FIG. 3. The evolution of the $Ni_{50}Mn_{45}In_5$ XRD spectra with increasing annealing time at 750 K. The figure focuses on the development of the cubic (400) and (422) peaks pertaining to the FM $Ni_{50}Mn_{25}In_{25}$.

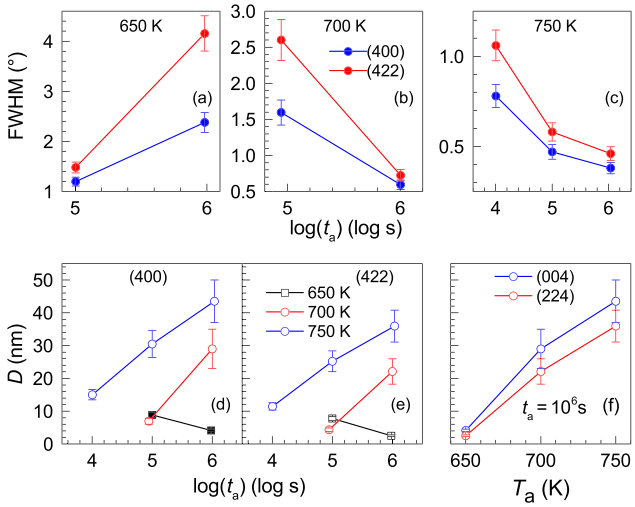

FIG. 4. The profile analysis of the (400) and (422) peaks and the evolution of the precipitate-size with time and temperature. FWHM for (a) T_a = 650 K, (b) T_a = 700 K, and (c) T_a = 750 K. Logt_a-dependence of D determined from (d) the (400) peak and (e) the (422) peak. (d) T_a-dependence of D determined from both peaks.

is then roughly 1.2-2. For larger diameters, namely for those formed at $T_a > 650$, the shell-FM effect becomes masked by the volume effect. This initial study on the size-determination of shell-FM precipitates requires further studies with microscopy and small angle x-ray and neutron scattering techniques.

Work supported by the Deutsche Forschungsgemeinschaft (SPP 1599).

[1] A. Planes, L. Mañosa, and M. Acet, J. Phys.: Condens. Matter **21**, 233201 (2009).
[2] O. Söderberg, A. Sozinov, Y. Ge, S. P. Hannula, and V. K. Lindroos, in *Handbook of Magnetic Materials* (2006), Vol. 16, pp. 139.
[3] R. Kainuma, Y. Imano, W. Ito, Y. Imano, W. Ito, Y. Sutou, H. Morito, S. Okamoto, O. Kitakami, K. Oikawa, A. Fujita, T. Kanomata, and K. Ishida, Nature (London) **439**, 957 (2006).
[4] V. Franco, J. S. Blázquez, B. Ingale, and A. Conde, Annu. Rev. Mater. Res. **42**, 305 (2012).
[5] J. Liu, T. Gottschall, K. P. Skokov, J. D. Moore, and O. Gutfleisch, Nat. Mater. **11**, 620 (2012).
[6] S. Chatterjee, S. Giri, S. Majumdar, and S. K. De, J. Phys. D: Appl. Phys. **42**, 065001 (2009).
[7] V. K. Sharma, M. K. Chattopadhyay, and S. B. Roy, Phys. Rev. B **76**, 140401(R) (2007).
[8] R. Y. Umetsu, X. Xu, W. Ito, T. Kihara, K. Takahashi, M. Tokunaga, and R. Kainuma, Metals **4**, 609 (2014).
[9] B. M. Wang, Y. Liu, P. Ren, B. Xia, K. B. Ruan, J. B. Yi, J. Ding, X. G. Li, and L. Wang, Phys. Rev. Lett. **106**, 077203 (2011).
[10] Z. D. Han, B. Qian, D. H. Wang, P. Zhang, X. F. Jiang, C. L. Zhang, and Y. W. Du, Appl. Phys. Lett. **103**, 172403 (2013).
[11] A. Cakir, M. Acet, and M. Farle, Phys. Rev. B **93**, 094411 (2016).
[12] A. Cakir, M. Acet, and M. Farle, Sci. Rep. **6**, 28931 (2016).
[13] D. L. Schlagel, R. W. McCallum, and T. A. Lograsso, J. Alloys Compd. **463**, 38 (2008).
[14] W. M. Yuhasz, D. L. Schlagel, Q. Xing, K. W. Dennis, R. W. McCallum, and T. A. Lograsso, J. Appl. Phys. **105**, 07A921 (2009).
[15] W. M. Yuhasz, D. L. Schlagel, Q. Xing, R. W. McCallum, and T. A. Lograsso, J. Alloys Compd. **492**, 681 (2010).
[16] K. Niitsu, K. Minakuchi, X. Xu, M. Nagasako, I. Ohnuma, T. Tanigaki, Y. Murakami, D. Shindo, and R. Kainuma, Acta Mater. **122**, 166 (2017).
[17] C. Felser, L. Wollmann, S. Chadov, G. H. Fecher, and S. S. P. Parkin, APL Mater. **3**, 041518 (2015).
[18] A. Cakir, Shell Ferromagnetism, https://www.youtube.com/watch?v=0VlSksW2G-s.
[19] A. Cakir, Perpendicular anisotropy of a shell ferromagnet https://www.youtube.com/watch?v=v4OiTxPnSkY.
[20] V. Petricek, M. Dusek, and L. Palatinus, Z. Kristallogr. **229**(5), 345 (2014).
[21] A. Cakir, M. Acet, U. Wiedwald, T. Krenke, and M. Farle, Acta Mater. **127**, 117 (2017).
[22] T. Krenke, A. Cakir, F. Scheibel, M. Acet, and M. Farle, J. Appl. Phys. **120**, 243904 (2016).
[23] F. Scheibel, D. Spoddig, R. Meckenstock, A. Cakir, M. Farle, and M. Acet, AIP adv. **7**, 056425 (2017).
[24] A. Cakir, M. Acet, U. Wiedwald, T. Krenke, and M. Farle, Acta Materialia **127**, 117–123 (2017).